Thin-Walled Structures 188 (2023) 110874

Contents lists available at ScienceDirect

Thin-Walled Structures

journal homepage: www.elsevier.com/locate/tws

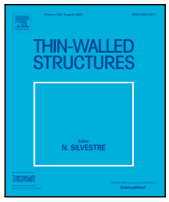

Full length article

Experimental investigation of the air blast performance of hybrid composite skinned sandwich panels with X-ray micro-CT damage assessment

E. Rolfe [a], R. Quinn [a], G. Irven [a,b], D. Brick [c], R.E. Johnston [d], J.P. Dear [a], H. Arora [e,*]

[a] Department of Mechanical Engineering, Imperial College London, London, SW7 2AZ, United Kingdom
[b] FAC Technology, 53 Lydden Grove, Wandsworth, London, SW18 4LW, United Kingdom
[c] Radnor Range Ltd, 11 Broadaxe Business Park, Presteigne, LD8 2UH, United Kingdom
[d] Advanced Imaging of Materials Centre, Faculty of Science and Engineering, Swansea University, Swansea, SA1 8EN, United Kingdom
[e] Department of Biomedical Engineering, Swansea University, Swansea, SA1 8EN, United Kingdom

ARTICLE INFO

Keywords:
Air blast
Composite sandwich panel
Hybrid composite
Digital image correlation
X-ray micro-CT

ABSTRACT

This research investigates the performance of interlaminar hybrid composites as the skins of composite sandwich panels under blast loading with the aim of promoting delamination between dissimilar plies for energy absorption. The deformation of the composite panels was captured using high-speed digital image correlation (DIC). High-speed full-field DIC enables failure to be captured at the moment it occurs across the entire panel. X-ray micro-CT imaging was used to assess the post-blast damage sustained by particular areas of interest from each panel, which were selected based on DIC results. The combination of full-field DIC and detailed X-ray micro-CT scanning enabled a unique comparison of both the global and localised blast resilience of hybrid and conventional composite sandwich panels to be performed.

Following a single blast load, the extent of damage to the Hybrid-3B skinned sandwich panel was found to lie between that of GFRP and CFRP skinned sandwich panels. X-ray micro-CT scanning of these panels reveals that there is no continuous damage path through the skin thickness of Hybrid-3B, whereas the GFRP and CFRP panels sustain damage in every ply.

Following repeat blast loading, the Hybrid-4 skinned sandwich panel suffered from a front skin crack spanning the length of the panel. Post-blast compressive strength testing reveals that this skin crack and resulting core crack acted as a stress relief, limiting the damage sustained elsewhere in the panel.

It was concluded that Hybrid-3B results in a good trade-off between strength and stiffness and is advantageous over conventional CFRP and GFRP panels under a single blast load. Under repeated loading Hybrid-4 offers advantages over Hybrid-3B. Finally, the design of the support structure can significantly aid in blast resilience, and, a holistic approach considering both panels and support should be taken when designing for blast resilience.

1. Introduction

Composite sandwich panels are being adopted for an increasing number of engineering applications. The performance advantages that composite materials possess, in the marine and naval industry, lead to enhanced stealth properties, higher velocity or greater payload, and reduced maintenance costs [1]. Naval vessels are also required to withstand a range of demanding loads due to the environment in which they operate. This can include impact, wave slamming and both air and underwater blast loading. Blast loading phenomena are complex and can result in devastating consequences. Therefore, composite material behaviour against blast loads must be investigated further to achieve the necessary performance and safety standards.

Numerous experimental and numerical investigations on blast performance of composite sandwich panels have been carried out [2–4]. For a comprehensive review of recent research into blast performance of fibre-based polymer composites, the reader is directed to Ref. [5]. Researchers have widely concluded that the core material absorbs most of the energy during blast [6] and investigations focussing on the core material have been performed [2,4,7]. However, the composite skins provide in-plane and bending stiffness to the structure following a blast load. Improving blast resilience of the composite skins is equally important. Investigations into skin resilience during blast have been performed [8–11]. Arora et al. [12] compared the large-scale blast performance of composite sandwich panels with glass-fibre reinforced polymer (GFRP) and carbon-fibre reinforced polymer (CFRP) skins. The

* Corresponding author.
E-mail address: hari.arora@swansea.ac.uk (H. Arora).

https://doi.org/10.1016/j.tws.2023.110874
Received 17 May 2022; Received in revised form 9 February 2023; Accepted 14 May 2023
Available online 3 June 2023
0263-8231/© 2023 The Authors. Published by Elsevier Ltd. This is an open access article under the CC BY license (http://creativecommons.org/licenses/by/4.0/).

GFRP sandwich panel suffered from a large front skin crack and underwent greater panel deflection. However, the reduction in relative load bearing capacity after blast was greater in CFRP targets demonstrating potential for a trade-off between the two composite materials.

The use of polymer interlayers within composite laminate skins to increase energy absorption has been investigated following a successful demonstration that poly-urea (PU) interlayers improve the properties of concrete structures under blast loading [13]. Kelly et al. [7] determined that a composite sandwich panel with GFRP skins and polypropylene (PP) interlayers improved the energy storage capacity of the GFRP by preventing front face sheet failure. Panels deflected less than a panel with solely GFRP skins and an identical core when simultaneously subjected to the same blast load. Upon post-blast inspection the panel with PP interlayers suffered from less front skin/core debonding and had no front skin cracks. Gardner et al. [14] have performed shock tube investigations studying the addition of PU interlayers within composite sandwich panels. The position of the interlayer was found to affect deflection and strain of the sandwich panels. Placing the interlayer behind the front skin or behind the core was found to reduce deflection, velocity and in-plane strain. The concept of using polymer interlayers can be extended to the use of hybrid composite laminates as sandwich panel skins. Hybrid composites are being widely researched with the aim of improving toughness of composite materials along with improving damage resistance and reducing brittle modes of failure. These properties would be beneficial under blast loading.

The impact performance of simple hybrid composites, using materials that are commercially available, has been widely researched. Impact performance has been linked to toughness [15]. Key investigations performed by Sevkat et al. [16,17] found that damage accumulation was reduced when glass-fibre layers were the outside layers in GFRP/CFRP hybrid laminates under impact. The authors attributed this to the incompatibility of the layers increasing the likelihood of delamination. Other authors have separately reached similar conclusions, that impact resistance is improved when glass-fibre fabrics were the outermost layer experiencing impact [18–20].

The ability of hybrid composites to exhibit damage contributes directly to the amount of energy they could absorb under impact loading. Park and Jang [21] compared the impact performance of interlayer and intralayer aramid-fibre and polyethylene (PE) fibre hybrids. The authors observed that the interlayer hybrids had a greater penetration resistance due to the easier development of a delamination. However, this led to greater delaminated areas and should result in poorer post-impact mechanical properties.

Czél et al. [22] have successfully controlled the damage mechanisms by reducing the thickness of the low elongation carbon-fibre layer. The authors sandwiched a 29 μm carbon-fibre layer between thicker glass-fibre layers. Under tensile testing, this led to several breaks in the carbon-fibre along the length of the sample with diffuse delamination before the glass-fibre layers broke. This failure mechanism absorbed a significant amount of energy. Wisnom et al. have continued to perform investigations into thin-ply carbon/glass hybrid composites [23,24], including under bending which is most relevant to this study [25]. The authors tested thin-ply hybrids under 4-point bending, making use of asymmetric layups, and achieved gradual failure with high levels of flexural displacement. The specimens exhibited no catastrophic failure but rather progressive brush-like failure. By identifying the failure sequence of the plies, the authors were able to identify an optimum architecture.

With regards to blast loading, there exists an optimum architecture to achieve the best possible trade-off between energy absorption through damage mechanisms and post-blast performance. Previous large-scale blast testing of hybrid composite sandwich panels [26,27] demonstrated that hybrid skins advantageously reduce the panel deflection compared to sandwich panels with conventional GFRP or CFRP skins. However, the position of the glass-fibre and carbon-fibre layers was shown to have no effect under such large-scale testing unlike during localised impact testing [28].

Table 1
Details of the panel types tested in each series.

Test series	PE7 charge (kg)	Stand-off distance (m)	Panel type
A	30	10.5	GFRP CFRP Hybrid-3B(1)
B	8	8	Hybrid-3B(2) Hybrid-4(1)

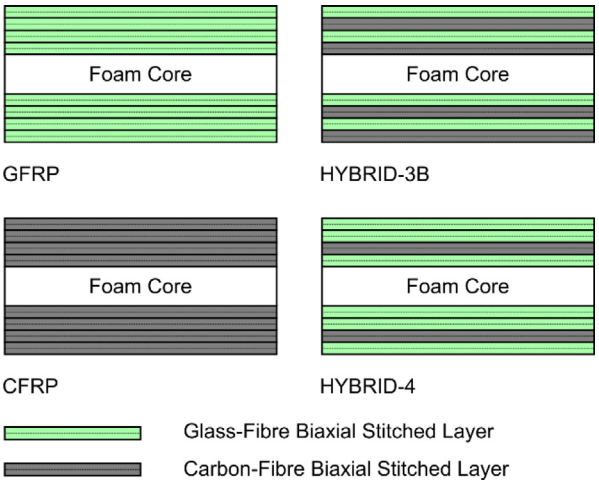

Fig. 1. Schematic layup diagram of composite sandwich panels.

This paper aims to extend the preceding research by investigating hybrid composite sandwich panels with more significant differences in layup and thinner carbon-fibre layers to promote energy absorbing delamination failures observed by other researchers [22]. Furthermore, this paper utilises a combination of full-field DIC and detailed X-ray micro-CT scanning to perform a comparison of the global and localised blast resilience between hybrid and conventional composite sandwich panels.

2. Materials

The performance of composite sandwich panels, with both hybrid skins and conventional skins, were analysed during two test series. A schematic diagram showing the layups of these panels is shown in Fig. 1. During test series A, three panels were subjected to a 30 kg PE7 charge at 10.5 m stand-off distance. Test series B involved subjecting two hybrid panels to a repeat blast load. The panels underwent two 8 kg PE7 charges at 8 m stand-off distance. The types of panels evaluated in each test are detailed in Table 1.

All panels were 1.39 m × 1.23 m in size. The panels were constructed from four layers of bi-axial fabric either side of a 30 mm thick Divinycell H100 PVC foam core. The fabric layers were arranged quadriaxially, $[0/90/-45/+45]_2$ CORE$[+45/-45/90/0]_2$. Gurit XE603 600 gsm E-glass fibre and 400 gsm HexTow AS4 carbon-fibre were used. The panels were infused with a mix of SR8100 epoxy resin and SD8824 hardener. The panels were fabricated using resin infusion. The panels were ambient cured and then held under vacuum for 24 h before being demoulded. The panels were manufactured by Independent Composites in Bristol.

For test series A, GFRP, CFRP and Hybrid-3B panels were selected. The GFRP and CFRP panels would act as benchmarks and quantify the advantages or disadvantages of adopting a hybrid skin under the same blast conditions. Hybrid-3B was selected as it was constructed from an equal number of plies of glass-fibre and carbon-fibre. Thereby sitting between the GFRP and CFRP panels in mass. Although this one layup

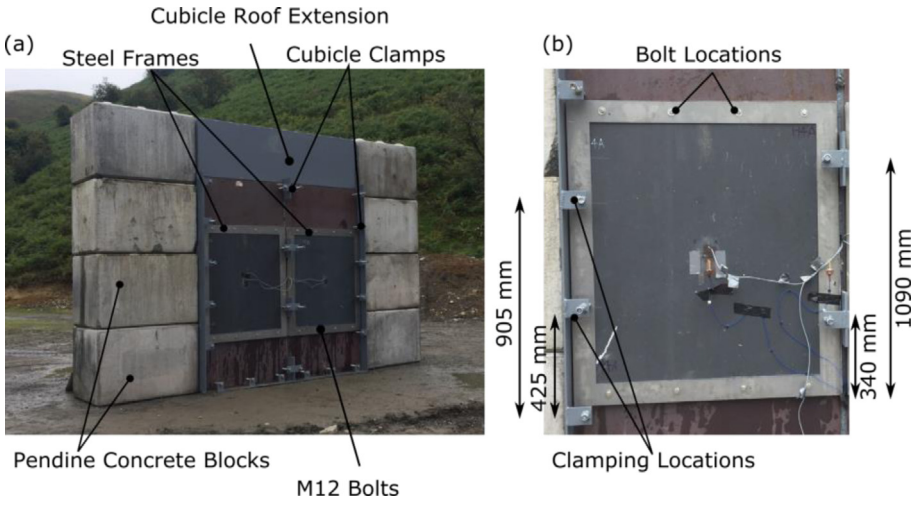

Fig. 2. Photographs of panels mounted on the cubicle.

Table 2
Properties of the composite sandwich panels.

Panel type	Areal density (kg m^{-2})	Equivalent bending stiffness (kN m^{-2})	Fibre volume fraction
GFRP	10.21	19.8	0.55
CFRP	8.98	55.5	0.46
Hybrid-3B	9.94	48.7	0.39
Hybrid-4	9.88	38.9	0.39

of an equally distributed number of plies of carbon-fibre and glass-fibre was selected, the choice of layup is acknowledged to influence performance [28]. Due to test limitations a selection was made to use Hybrid-3B for this test series.

For test series B, Hybrid-3B and Hybrid-4 panels were compared. This was to identify the change in performance achieved by varying the hybrid skin layup. Hybrid-4 contains a greater proportion of glass-fibre, reducing the panel bending stiffness but also reducing the number of interfaces between the dissimilar glass-fibre and carbon-fibre layers. Table 2 details properties for each panel type. The areal density was calculated from the mass and dimensions of the manufactured panels. The bending stiffness was calculated using classical beam theory, datasheet properties and the thickness of each layer measured from the manufactured panels. Fibre volume fraction was calculated using thickness of each layer measured from the manufactured panels and the fibre and areal densities of the dry fibres provided by the manufacturers.

3. Methods

3.1. Air blast experimental method

During testing, the composite sandwich panels were mounted side-by-side onto the front of a steel cubicle. The panels were bolted to the cubicle along the top and bottom edges using 8 × M12 bolts and clamped along the vertical edges in four positions. The bolts were equally spaced 154 mm and 462 mm either side of the centre line along the top and bottom edges. The position of the clamping locations are shown in Fig. 2(b). A 100 mm wide, 5 mm thick steel frame was placed up against the panel to help distribute the bolting and clamping forces.

Pendine concrete blocks were placed alongside the cubicle to reduce blast clearing effects. Clearing is where the blast wave passes around the free edge of a structure, which can lead to a reduced amplitude and duration of loading on the target. The reader is directed to Rigby et al. [29] for a detailed explanation of blast clearing effects. In addition, the vertical height of the cubicle was extended using a steel sheet supported by welded struts. These blocks and height extension aimed to mitigate the effects of blast clearing around the cubicle. Fig. 2 shows an image of the cubicle setup with two panels mounted prior to testing and a more detailed view of the fixing locations. The stand-off distances for the experiments were calculated, using the method outlined by Andrews and Moussa, to cause core damage and limited front skin damage [30], and Computational Fluid Dynamics (CFD) modelling detailed in Section 3.2. Fig. 3 shows a schematic diagram of the test pad setup. The spherical PE7 charge for each experiment was positioned on a polystyrene stand in-line with the mid-height of the panels and at the perpendicular stand-off distance, illustrated in Fig. 3, as specified in Table 1.

3D DIC was implemented to capture the response of the panels during blast loading. Since two panels were tested per charge, four high-speed cameras were used. The cameras used were a pair of Photron SAX2s and a pair of Photron AX100s recording at 12,500 fps and 4000 fps, respectively. The cameras were triggered via a manual switch which was pressed at the same time as the charge detonation switch. For this study, 24 mm lenses were used on all cameras to ensure the panels were within the field of view (FOV). The cameras were mounted vertically on a heavy-duty camera stand, weighed down with sandbags for further ballast. Banks of LED lights were used to illuminate the back skin of the panels during blast testing. Fig. 4 shows the setup of the high-speed cameras within the cubicle mounted in vertical pairs. Camera calibration was carried out using a 700 mm CC coded calibration cross supplied by GOM UK. A speckle pattern was painted on the back skin of each panel to facilitate DIC. During test series A, an additional high-speed Photron SA1 camera was setup to record the progression of the wave front. This camera was mounted on the bank of the test arena.

Polyvinylidene fluoride (PVDF) film pressure sensors were implemented during the blast experiment. A PVDF sensor was taped to the centre of each panel for all blast experiments. Movement of the sensor cable was minimised by fixing it to the panel and cubicle by using self-adhesive cable ties. The pressure gauges were connected via a charge amplifier to the data acquisition setup. The PVDF pressure sensors measure the pressure as the air particles come to rest against the panel surface, which is the reflected overpressure. To validate blast calculations, a side-on pressure gauge was situated at the set stand-off distance for each test, 10.5 m for test series A and 8 m for test series B. The side-on pressure gauge was positioned at the centre height of the charge and parallel to the blast wave. This measured the static overpressure as the air particles moved over the face of the pressure sensor. To reduce the disruption of the flow a thin steel plate was placed over the sensor face.

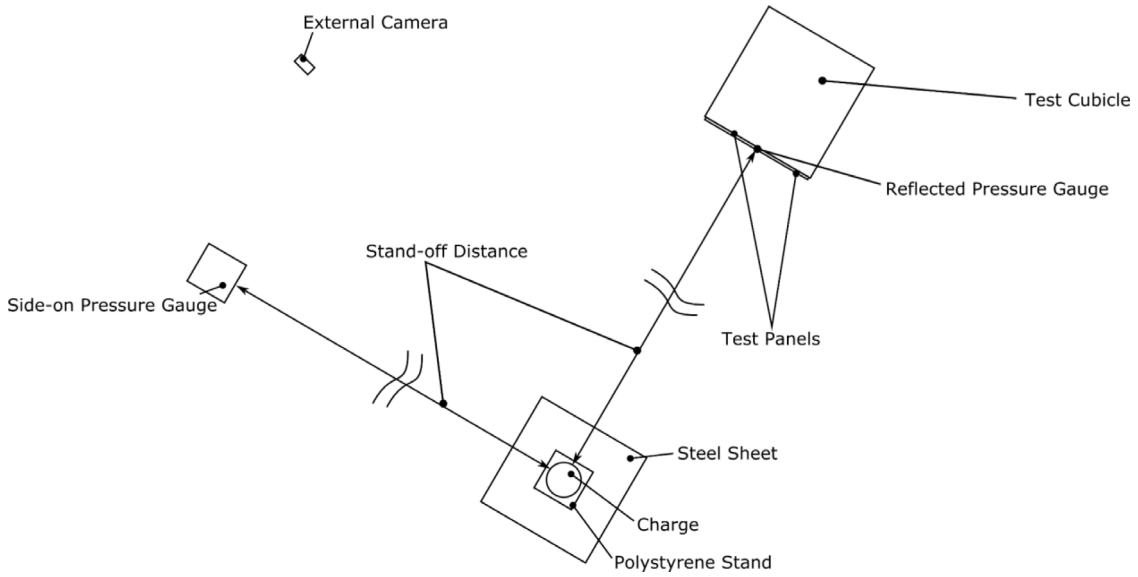

Fig. 3. Schematic of the test pad setup showing locations of pressure gauges.

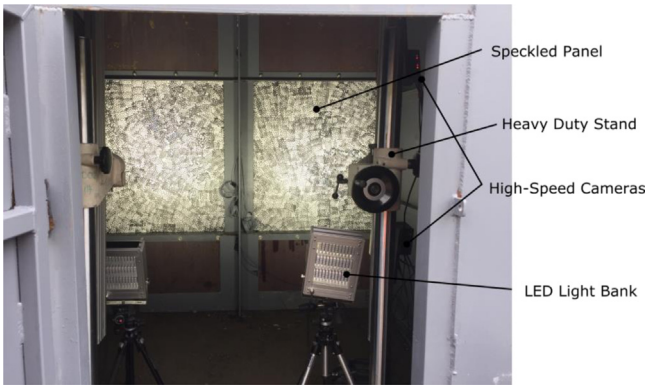

Fig. 4. Photograph showing the DIC setup within the test cubicle.

3.2. Computational fluid dynamics modelling

To support the analytical stand-off distance calculations performed and to generate numerical data to supplement experimental results, a CFD model of the experimental setup was created using Pro S Air. The analytical method assumes a uniform pressure across the panel front. In reality the pressure distribution across the panel front varies due to blast clearing effects despite the cubicle modifications and Pendine concrete blocks adopted as mitigation.

It is only possible to define infinitely rigid obstacles in the CFD solver as it has no structural capabilities. Nevertheless, the results provide an estimate of the reflected overpressure across the test panels. A spherical geometry, cylindrical geometry and 3D geometry were used in turn to efficiently model the separate stages of the blast wave and its interactions with the surroundings. Each geometry stage had an appropriate cell size and problem time as recommended both by the software user guides [31,32], and by convergence studies performed in previous investigations [33]. The spherical geometry modelled the pressure from detonation until the blast wave reached the closest boundary, the floor. The cylindrical geometry modelled the blast wave between reaching the floor and reaching the next boundary, the cubicle. The 3D geometry stage took over to model the blast wave as it encountered the 3D test cubicle as an object. For computational efficiency, a plane of symmetry was assumed to run through the centre of the test cubicle. This symmetry boundary was assumed to be reflective along with the floor with 100% of the blast energy being reflected. All other boundaries were 100% transmissive. In the 3D geometry stage, the control volume that was modelled spanned from the ground to 4 m in height, from the centre of the charge to 13.5 m or 11.5 m in length, depending on the stand-off distance, and from the centre of the cubicle to 4 m in width. The reflected overpressure was measured 25 mm in front of the cubicle to take into account the panel thickness. It is acknowledged that taking measurements at this location results in an underestimation of the overpressure. A measurement was taken at 400 target points across the panel. Pro S Air only had the capability to model PE4 not PE7. However, considering both plastic explosives consist of 88% Research Department Explosive (RDX) and have the same TNT equivalent, the difference was deemed negligible. The model was used to verify test setup parameters and guide post-test analysis.

3.3. Post-blast damage analysis

Visual inspection, residual strength tests and detailed X-ray micro-CT imaging was performed to study damage. Following blast testing, the damage sustained by each panel was recorded and evaluated to reveal differences in the blast resilience of the panel layups. The panels were sectioned. All edges were photographed and visually inspected for core cracks, front skin/core debonding and rear skin/core debonding. The damage types and extent of damage was recorded. Ten 300 mm × 200 mm specimen were taken from each panel and subjected to edgewise compression loading. Other types of loading were considered, however, edgewise compression loading was selected as all damage types sustained by the panels during blast loading would be exacerbated by this load direction leading to catastrophic failure via buckling. The aim was to discern the impact of various degrees of perceived damage from visual inspection on residual load bearing capacity and likelihood of failure. Edgewise compression would simulate the structural loads experienced by the panel in service if used as part of a vessel superstructure or hull. Furthermore, the compressive strength of composite laminates is considerably lower than their tensile strength. Therefore, compressive strength is usually the critical design criteria [34]. Testing was performed using an Instron 5985 universal testing machine at a quasi-static test rate of 2 mm min^{-1}. A Nikon D7100 DSLR camera was used to capture one photograph every second

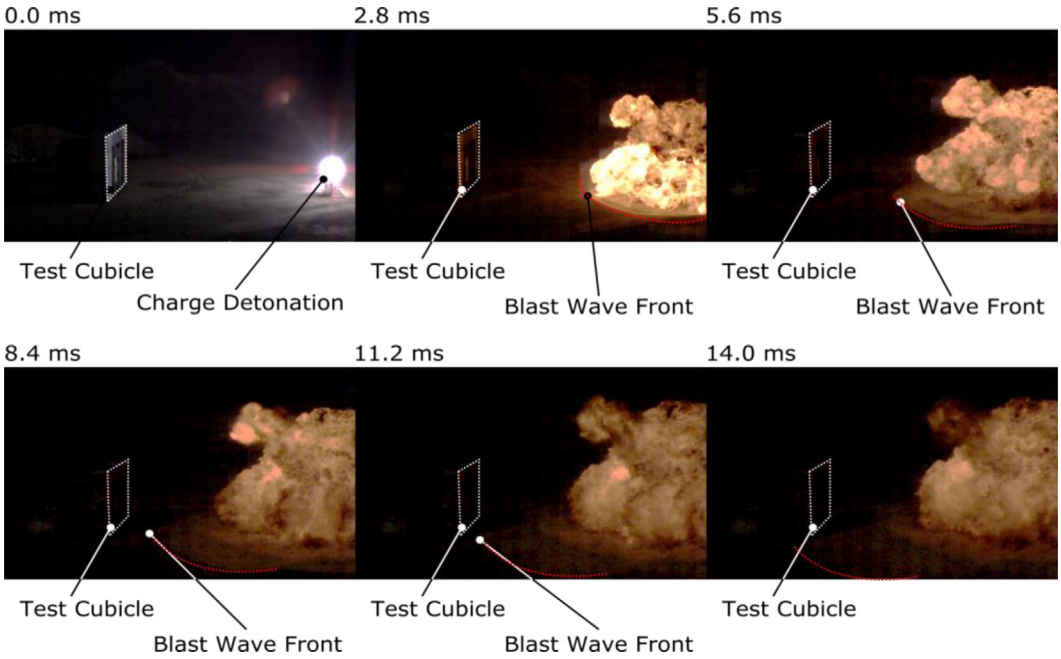

Fig. 5. Photographs showing the detonation of the charge and progression of the blast wave front.

to measure the strain using 2D DIC. A speckle pattern was painted along one edge of each specimen to facilitate DIC. To ensure even loading, 10 mm thick rubber spacers were placed between the machine platens and the steel plates. 2D DIC was adopted due to potential slipping at the platens resulting in inaccurate machine displacement readings. The 2D DIC data was used to calculate the initial specimen modulus prior to the onset of appreciable out-of-plane displacement. An effective edgewise stiffness was calculated from the in-plane engineering stress and average strain.

Further analysis of damage type and severity sustained by each skin layup was performed using X-ray micro-CT imaging. Highly damaged, 20 mm × 20 mm, samples were taken from each panel after blast testing. This sample size was selected in order to capture the required level of detail and optimise scanning efficiency. Two lab-based X-ray micro-CT/microscopy systems were used for imaging the samples. Scans of the CFRP and GFRP samples were carried out using a lab-based Nikon XT H225 microfocus X-ray microtomography system, with a 1.3 Megapixel Varian PaxScan 2520 amorphous silicon flat panel digital X-ray imager in reflection mode with a tungsten target. An X-ray tube voltage of 60 kV, and a tube current of 65 μA were used, with an exposure of 500 ms. A total of 3015 projections were captured with a voxel (3D pixel) size of 17.46–17.85 μm. The tomograms were reconstructed from 2D projections using a Nikon commercial software package (CTPro version 3.0, Nikon Metrology), a cone-beam reconstruction algorithm based on filtered back-projection. The commercial software VGStudio Max 2.1.5 was used to view the reconstructed data, produce 2D grayscale slices, and 3D volumes. Hybrid-3B(1), Hybrid-3B(2) and Hybrid-4(1) samples were investigated using a lab-based Zeiss Xradia 520 (Carl Zeiss XRM, Pleasanton, CA, USA) X-ray microscope, using a CCD detector system with scintillator-coupled visible light optics, and tungsten transmission target. An X-ray tube voltage of 100 kV, and a tube current of 90 μA were used, with an exposure of between 500–1000 ms, and a total of 3201 projections. An objective lens giving an optical magnification of 0.4× was selected with binning set to 2, producing anisotropic voxel (3D pixel) sizes in the range 16.888 μm to 30.150 μm. The tomograms were reconstructed from 2D projections using a Zeiss commercial software package (XMReconstructor, Carl Zeiss), a cone-beam reconstruction algorithm based on filtered back-projection. TXM3DViewer software was used to produce 2D grayscale slices for subsequent analysis.

4. Results & discussion

4.1. Air blast experimental results & discussion

4.1.1. Test series A: Hybrid-3B versus conventional GFRP and CFRP

The progression of the blast wave during test series A is shown in Fig. 5. The first image clearly shows the detonation of the spherical charge and the test cubicle. The blast wave front travelling across the ground can then be seen in the subsequent images. The camera exposure was set to a minimum to prevent overexposure caused by the detonation. This makes the final two images less clear. The blast wave can be seen reaching the cubicle between 11.2 ms and 14.0 ms after charge detonation, as predicted by Pro S Air simulations (11.7 ms). Since only two panels could be mounted on the cubicle during each experiment, GFRP and CFRP were subjected to the first charge. Hybrid-3B(1) was tested against the second charge.

Fig. 6(a) shows a sequence of contour images of the out-of-plane deflection and major strain for GFRP at intervals of time under the 30 kg PE7 blast load. The major strain reaches a maximum at the panel centre point of 1.46%. GFRP experiences a maximum central displacement of 77.6 mm at the centre point at a time of 15.75 ms. Both deflection and major strain, at this time, are spread over a central circular area. However, at later times up to 17.75 ms, the area of maximum deflection and major strain becomes non-circular and a band in the contour plots become visible, indicative of damage. This remaining band of high strain and displacement, after peak deflection, indicates permanent panel damage.

The sequence of contour images of out-of-plane displacement and major strain for CFRP are shown in Fig. 6(b). It is clear that CFRP experiences a lower deflection and strain compared to GFRP due to the higher stiffness of carbon-fibre skins. The deflection and strain images indicate a region of damage running vertically down the centre of the panel. The maximum central displacement point of CFRP is 61.4 mm and maximum central point major strain is 0.79%.

Fig. 6(c) shows the DIC contour image series for Hybrid-3B(1). The panel experiences an area of high strain towards the top right-hand side of the panel. The deflection and strain images indicate a region of damage running diagonally across the panel. The maximum displacement of the centre point is 68.0 mm and maximum major strain at the centre point is 0.96%.

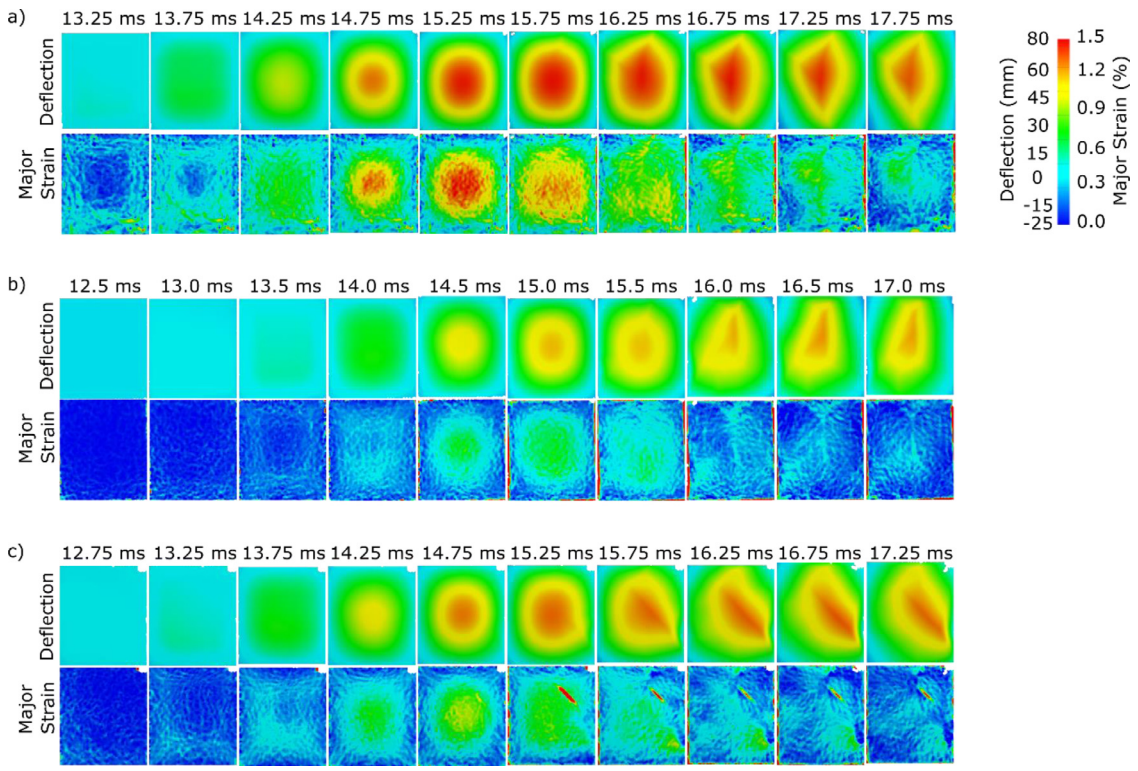

Fig. 6. DIC results for 30 kg PE7 charge at 10.5 m stand-off distance showing out-of-plane displacement and major strain contour images for: (a) GFRP, (b) CFRP and (c) Hybrid-3B(1).

Table 3
Summary of pressure gauge readings for test series A.

Panel type	Peak static overpressure (kPa)	Positive phase duration (ms)	Calculated reflected overpressure (kPa)	PVDF reflected overpressure (kPa)
GFRP	100.8	6.12	278.5	357.8
CFRP				320.6
Hybrid-3B(1)	93.8	12.23	253.3	334.5

Fig. 7 shows a plot of the static overpressure from the two trials along with the displacement of the centre points of all three panels. The static and reflected overpressures recorded by the two types of gauges during the first and second trial in test series A are detailed in Table 3. GFRP and CFRP were tested side-by-side, Hybrid-3B(1) was tested after. GFRP and CFRP experienced a peak static overpressure of 100.8 kPa whilst Hybrid-3B(1) experienced a peak static overpressure of 93.8 kPa. Considering the complexity of the field-based experiments, both the static overpressure results and reflected overpressure results reveal that the panels all experienced a peak pressure load within 10%. Hybrid-3B(1), however, undergoes a greater blast impulse due to a greater positive phase duration. These tests were performed one after the other, however, this change in phase duration could be caused by a change in atmospheric or weather conditions. Sources of experimental error could arise from variability in the charge, positioning of the charge or positioning of the side-on pressure gauge, however, precautions were made to minimise these effects, particularly with regards to positioning, where possible.

As expected, the deflection of the panels negatively correlates with their stiffness. The deflection of Hybrid-3B(1) lies between the deflections of GFRP and CFRP. CFRP demonstrates a double peak around its maximum deflection point. The timing of this double peak correlates with the development of the front crack that is visible in the major strain plots of Fig. 6(b) from 16.0 ms onwards. This corresponds with the three phases identified by Nurick et al. for uniform blast loading on panels with honeycomb cores [35]. The first CFRP peak here corresponds to the end of Phase 2, where the crush limit of the core is reached and front skin tearing initiates, albeit the front skin tearing in this case was at the panel centre not panel boundary. The second CFRP peak corresponds to Phase 3 where the tearing of the front skin further compresses the core, deforming the back skin and, in this case, releases residual momentum within the panel. Damage also causes the temporally elongated return of CFRP. Due to its high stiffness and low mass, CFRP should have the shortest time period of response followed by Hybrid-3B(1). Fig. 7 shows that this is not the case. The panel stiffness, or flexural rigidity, is reduced due to damage resulting in a longer period of response. This indicates that CFRP and Hybrid-3B(1) have suffered from greater overall panel damage compared to GFRP. Although Fig. 6(a) indicates that GFRP exhibits the highest strain and high strain across a greater region, GFRP is able to sustain greater strain before failure compared to CFRP. This widespread region of high strain in Fig. 6(a) does not mean that the GFRP panel has suffered from greater panel damage. However, failure mechanisms may differ which may impact residual load bearing capacity.

To evaluate the relative performance of the panels in terms of the blast energy dissipated, work done by each panel has been computed. The work done by each panel was calculated using both numerical and experimental data. The experimentally recorded peak static overpressure was used to calculate the peak reflected overpressure using the Rankine–Hugoniot relationship shown in Eq. (1). In this equation P_r is reflected overpressure, P_s is static pressure and P_o is ambient pressure. This relationship assumes the wave encounters an infinitely large rigid wall with a zero angle of incidence. The simulated reflected overpressure at 400 target points across the panel front was

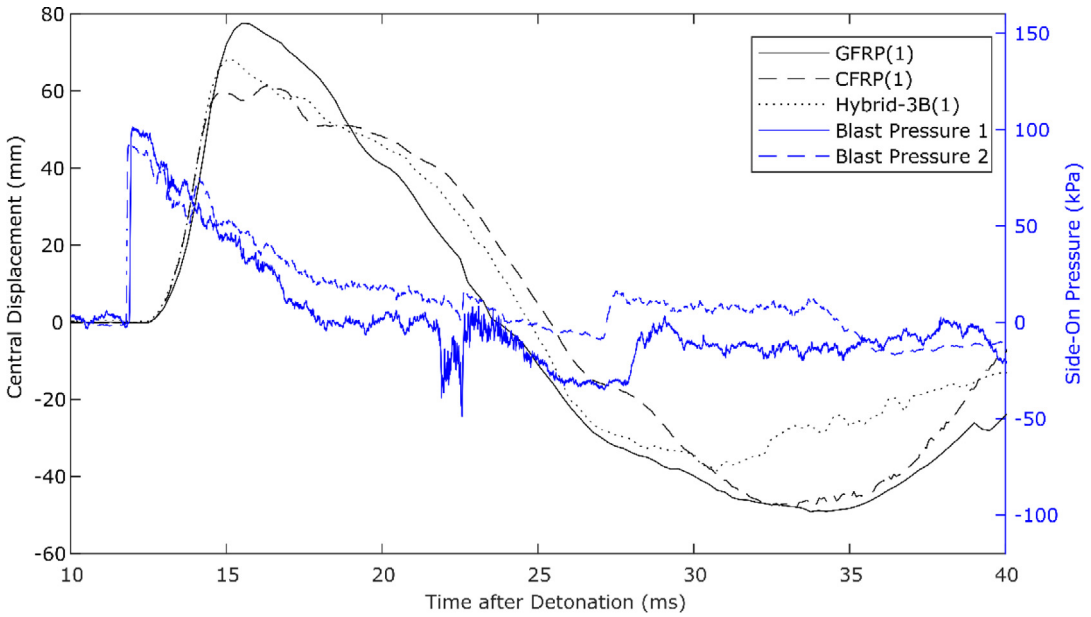

Fig. 7. Central out-of-plane displacement against time for composite panels under 30 kg PE7 charge at 10.5 m stand-off distance along with the recorded side-on blast pressure against time.

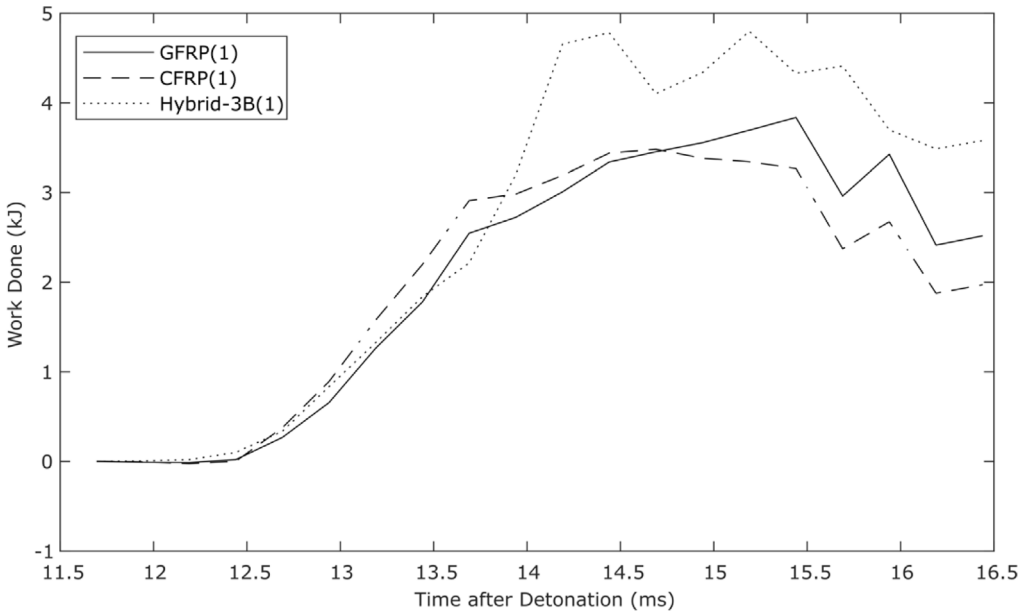

Fig. 8. Cumulative work done against time for composite panels under 30 kg PE7 charge at 10.5 m stand-off distance.

extracted from the CFD model detailed in Section 3.2. The overpressure at each target point and for each time step (between 11.75 ms and 16.25 ms) was normalised against the peak simulated reflected overpressure extracted from the CFD model. This resulted in normalised simulated values (between 0 and 1) for each target point at every time step. These simulated normalised pressures were multiplied by the experimentally calculated reflected overpressure. This results in a reflected overpressure distribution across the panel replicating the blast loading that occurred during the experiment. The displacement of the same 400 target points across the panel were extracted from DIC data for each time step. The work done at each point was calculated by multiplying the displacement at that point by the reflected overpressure experienced at that point and by the area encompassing that point. Fig. 8 shows a cumulative work done versus time plot for all three panels tested.

$$P_r = 2P_s\left[\frac{7P_o + 4P_s}{7P_o + P_s}\right] \tag{1}$$

Fig. 8 shows that GFRP and CFRP experience similar cumulative work done. Since these two panels were tested side-by-side and subjected to the same overpressure, this implies the panels experienced similar global displacements. Initially, the work done by GFRP is lower than the other two panels despite exhibiting a greater central point deflection. Therefore, the initial work done on CFRP must be caused by the deflection of a more widespread area. The work done by GFRP continues to increase and exceeds that of CFRP. This indicates that the deflection of GFRP is sustained for a longer period of time. Beyond 13.8 ms, Hybrid-3B(1) experiences the greatest work done. This is

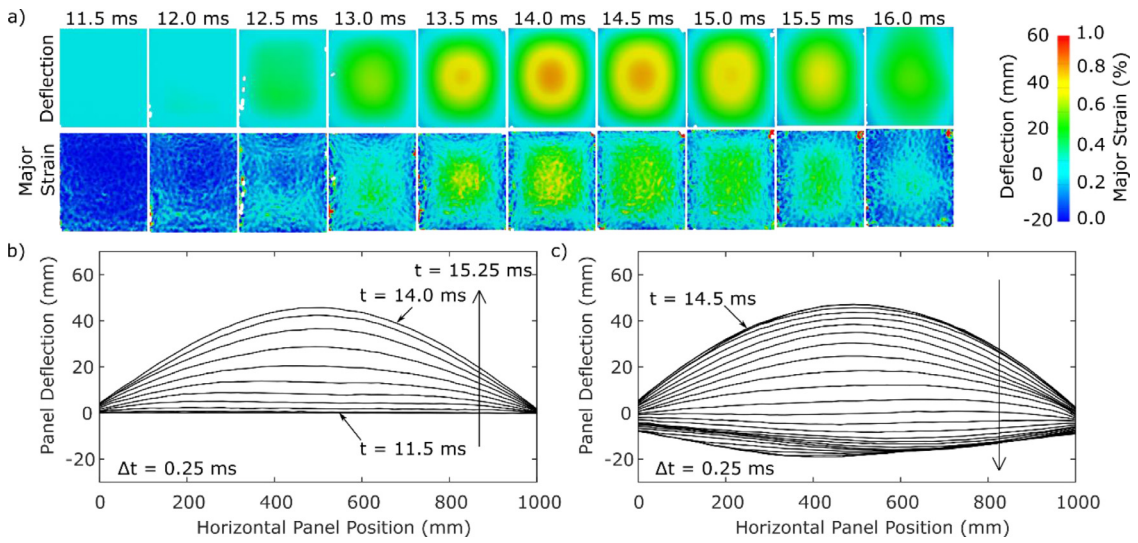

Fig. 9. DIC results for Hybrid-3B(2) under the first 8 kg PE7 charge at 8 m stand-off distance showing: (a) out-of-plane displacement and major strain images, (b) deflection at time intervals for the horizontal centre section and (c) rebound at time intervals for the horizontal centre section.

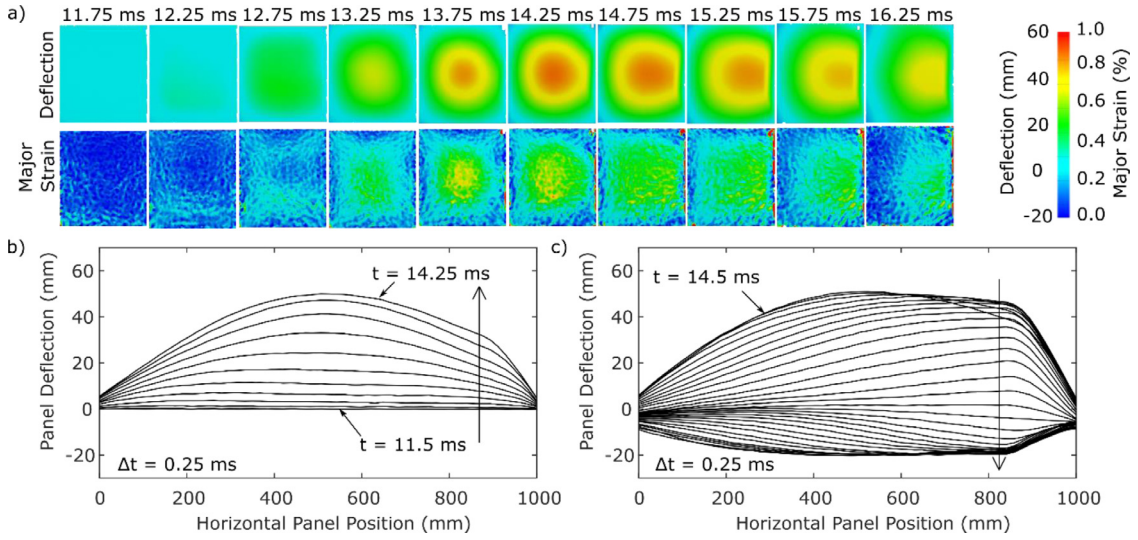

Fig. 10. DIC results for Hybrid-3B(2) under the second 8 kg PE7 charge at 8 m stand-off distance showing: (a) out-of-plane displacement and major strain images, (b) deflection at time intervals for the horizontal centre section and (c) rebound at time intervals for the horizontal centre section.

partially caused by the differing pressure signatures, shown in Fig. 7. This results in a greater impulse delivered to Hybrid-3B(1). The increased work done on Hybrid-3B(1) is also partially caused by the deflection of the panel. Fig. 7 shows that the centre point deflection of Hybrid-3B(1) lies between that of CFRP and GFRP, however, Fig. 6 shows a band of diagonal damage. Deflection in this band is greater than deflection at the centre point after approximately 15.25 ms. The increased work done by Hybrid-3B(1) is caused by a combination of the global panel deflection and the greater blast impulse due to the elongated decay of the second blast. Panel deflection can absorb a significant amount of blast energy and be beneficial for blast resilience, provided that the deflection does not cause excessive damage. Post-blast panel assessment will reveal whether the greater work done on Hybrid-3B(1), interrelated with its greater deflection, results in greater damage or whether the hybrid layup is advantageous.

4.1.2. Test series B: Hybrid-3B versus Hybrid-4 comparison

Fig. 9(a) shows a sequence of contour images of the out-of-plane displacement and major strain taken from DIC image processing for Hybrid-3B(2) under the first 8 kg PE7 blast load. The panel experiences a relatively symmetric outward deflection and return. Fig. 9(b) shows the displacement of the horizontal cross-section at the midplane of Hybrid-3B(2). The panel reaches a maximum central displacement of 47.2 mm at 14 ms and maximum central major strain of 0.66%. The symmetric response of the panel can be clearly seen in the cross-sectional displacement until the final few cross-sections of the return stroke. Deceleration is visible on the left-hand side of the panel, indicating the presence of damage. Fig. 10 shows the DIC data for the same panel, Hybrid-3B(2), under the second 8 kg PE7 blast load. The panel experiences a greater deflection with a maximum of 50.9 mm and maximum central major strain of 0.61%. The damage, caused by the first blast, results in an asymmetric deflection and the further accumulation of damage results in a more distorted return stroke.

Fig. 11 illustrates the response of Hybrid-4(1) to the first 8 kg PE7 blast load. Hybrid-4(1) experiences a greater central deflection and major strain compared to Hybrid-3B(2) under the first blast load with values of 51.9 mm and 0.78%, respectively. There is a greater extent of panel deceleration and a gradient discontinuity in the return stroke of Hybrid-4(1). The response of Hybrid-4(1) to the second blast load is shown in Fig. 12. The deflection and strain images in Fig. 12(a)

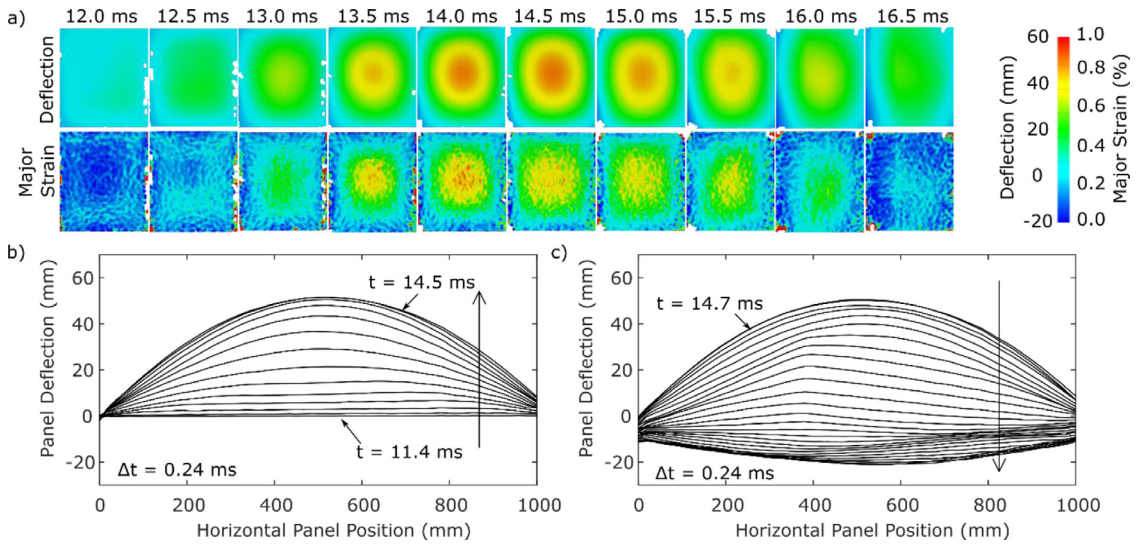

Fig. 11. DIC results for Hybrid-4(1) under the first 8 kg PE7 charge at 8 m stand-off distance showing: (a) out-of-plane displacement and major strain images, (b) deflection at time intervals for the horizontal centre section and (c) rebound at time intervals for the horizontal centre section.

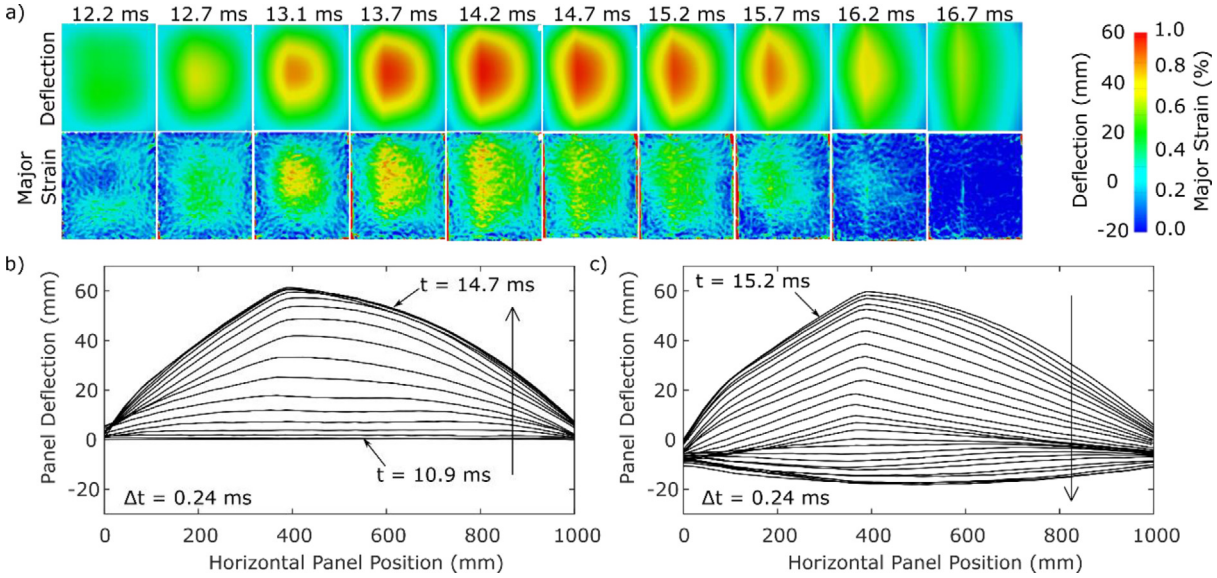

Fig. 12. DIC results for Hybrid-4(2) under the second 8 kg PE7 charge at 8 m stand-off distance showing: (a) out-of-plane displacement and major strain images, (b) deflection at time intervals for the horizontal centre section and (c) rebound at time intervals for the horizontal centre section.

indicate the location of a severe crack. The maximum central out-of-plane displacement of Hybrid-4(1) under the second blast load was 58.0 mm and maximum central major strain was 0.77%. Hybrid-4 has a lower equivalent bending stiffness compared to Hybrid-3B which is caused by a lower proportion of carbon-fibre layers in the layup. The results highlight that this reduced stiffness leads to greater panel deflection under air blast loading. The repeated blast loading increases the difference in performance between the two panels due to damage accumulation.

The work done on Hybrid-3B(2) and Hybrid-4(1) by the distributed blast pressures during the first and second trials in test series B have been calculated. The same method as previously detailed in Section 4.1.1 was used. Fig. 13 shows a plot of cumulative work done versus time for all four cases. Fig. 13 shows that Hybrid-3B(2) undergoes less work done during both trials compared to Hybrid-4(1). Since these panels were tested side-by-side and subjected to the same blast loads, this demonstrates that Hybrid-4(1) underwent greater global deflection.

The static overpressure recorded during each of the test series B blast trials is detailed in Table 4. The PVDF gauges failed to capture pressure data during the second trial as the amplifier gain for the second blast trial was set incorrectly. The voltage generated by the PVDF gauges, therefore, exceeded the cut off voltage for data acquisition. However other measurements indicate a highly comparable blast was delivered during the repeat test, see Table 4.

4.2. Post blast damage results & discussion

4.2.1. Test series A: Hybrid-3B versus conventional GFRP and CFRP

Fig. 14 shows the front views of GFRP, CFRP and Hybrid-3B(1) following sectioning. The red dashed boxes highlight the 300 mm × 200 mm regions that were removed from the panel for edgewise compression. All panels suffer from severe front skin fibre breakage. The front skin damage for all three panels correlates with the suspected damage observed in the DIC analysis. A DIC frame showing major strain around the peak displacement of each panel is shown alongside the panel front views in Fig. 14. The DIC data for both GFRP and CFRP

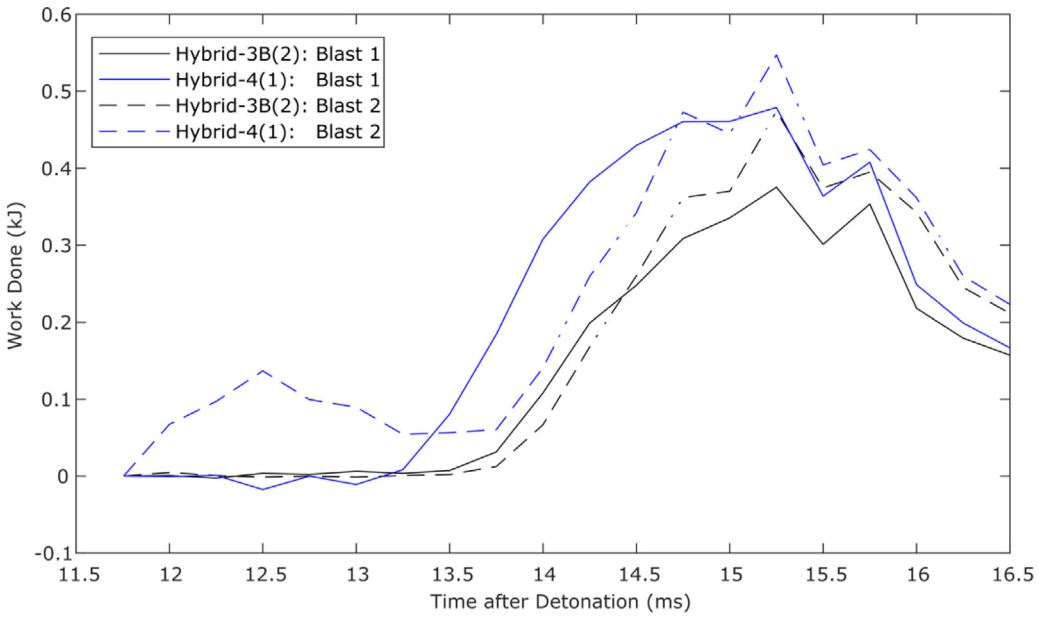

Fig. 13. Cumulative work done against time for the composite panels under 8 kg PE7 charge at 8 m stand-off distance.

Table 4
Summary of pressure gauge readings for test series B.

Trial number	Panel type	Peak static overpressure (kPa)	Positive phase duration (ms)	Calculated reflected overpressure (kPa)	PVDF reflected overpressure (kPa)
B1	Hybrid-3B(2) Hybrid-4(1)	68.1	5.01	172.1	305.8 310.4
B2	Hybrid-3B(2) Hybrid-4(1)	68.9	5.11	174.5	– –

Table 5
Visual inspection of damage sustained by the panels under 30 kg PE7 charge at 10.5 m stand-off distance.

Panel type	No. of core cracks	Length of core cracks (mm)	No. of core/front skin debonds	Length of front debonds (mm)	No. of core/rear skin debonds	Length of rear debonds (mm)	Length of front skin cracks (mm)
GFRP	11	426	6	243	4	129	2468
CFRP	14	448	4	72	1	44	2180
Hybrid-3B(1)	11	420	2	137	2	51	2958

show sharp gradient discontinuities and strain peaks at the panel centre which corresponds to the severe cracks running down the centre of the panels. GFRP also suffers from a diagonal crack towards the top of the panel. The DIC data for Hybrid-3B(1) highlights a crack running diagonally across the panel. This corresponds with the crack running from the bottom left-hand side of the panel to the middle right-hand side. The total length of the front skin cracks is detailed in Table 5.

Core shear cracks are visible approximately 150 mm in from the panel edges on all panels. The shear cracks occur at 45° to the through thickness direction. Fig. 15(b) shows cross-sections of Hybrid-3B(1) as viewed from the bottom of the panel. Fig. 15(c) highlights a cross-section where a shear core crack and debonding is visible. Many core shear cracks occur at this location as this is the transition region between the constrained edge and the deflecting central region.

Despite undergoing differing central point deflections, all three panels experience a similar extent of core shear cracking and front skin damage. GFRP suffers from greater front skin and core debonding. This is likely due to the reduced stiffness of the glass-fibre skins allowing greater deflection compared to the core. The extent of damage to Hybrid-3B(1) lies between that of GFRP and CFRP. Considering Hybrid-3B(1) underwent more widespread deflection and was subjected to a greater impulse, the ability for Hybrid-3B(1) to only sustain comparable levels of damage demonstrates that this hybrid layup is advantageous.

Fig. 16 shows the compressive strength for the specimens taken from the highlighted locations on GFRP, CFRP and Hybrid-3B(1). As mentioned previously, compressive strength is often the critical design criterion in structural naval composites. Specimens with no visually identifiable damage or one isolated type of damage sit above the dashed line shown in Fig. 16. Specimens with multiple damage types in more than one location have a reduced post-blast compressive strength and sit below this line. There is no clear correlation between the location from which the specimens were taken, e.g. proximity to panel centre, and the compressive strength achieved as shown in Fig. 17. The mean compressive strengths for GFRP, CFRP and Hybrid-3B(1) are 79.7 MPa, 86.1 MPa and 96.7 MPa, respectively. Additionally, the compressive strength ranges for GFRP, CFRP and Hybrid-3B(1) are 76.3 MPa, 85.3 MPa and 73.9 MPa, respectively. As previously hypothesised [12], the higher stiffness of the CFRP panel results in a faster wave speed allowing the wave propagation to the boundaries quicker than in the GFRP panel. This would lead to damage build up across the whole CFRP panel, however, under these conditions the increased stiffness of the CFRP panel has a detrimental effect. This more equal distribution does not occur as evidenced by a greater range of compressive strength results. Additionally, the mean compressive strength for CFRP is only 8% greater than that of GFRP. Although no undamaged specimens were

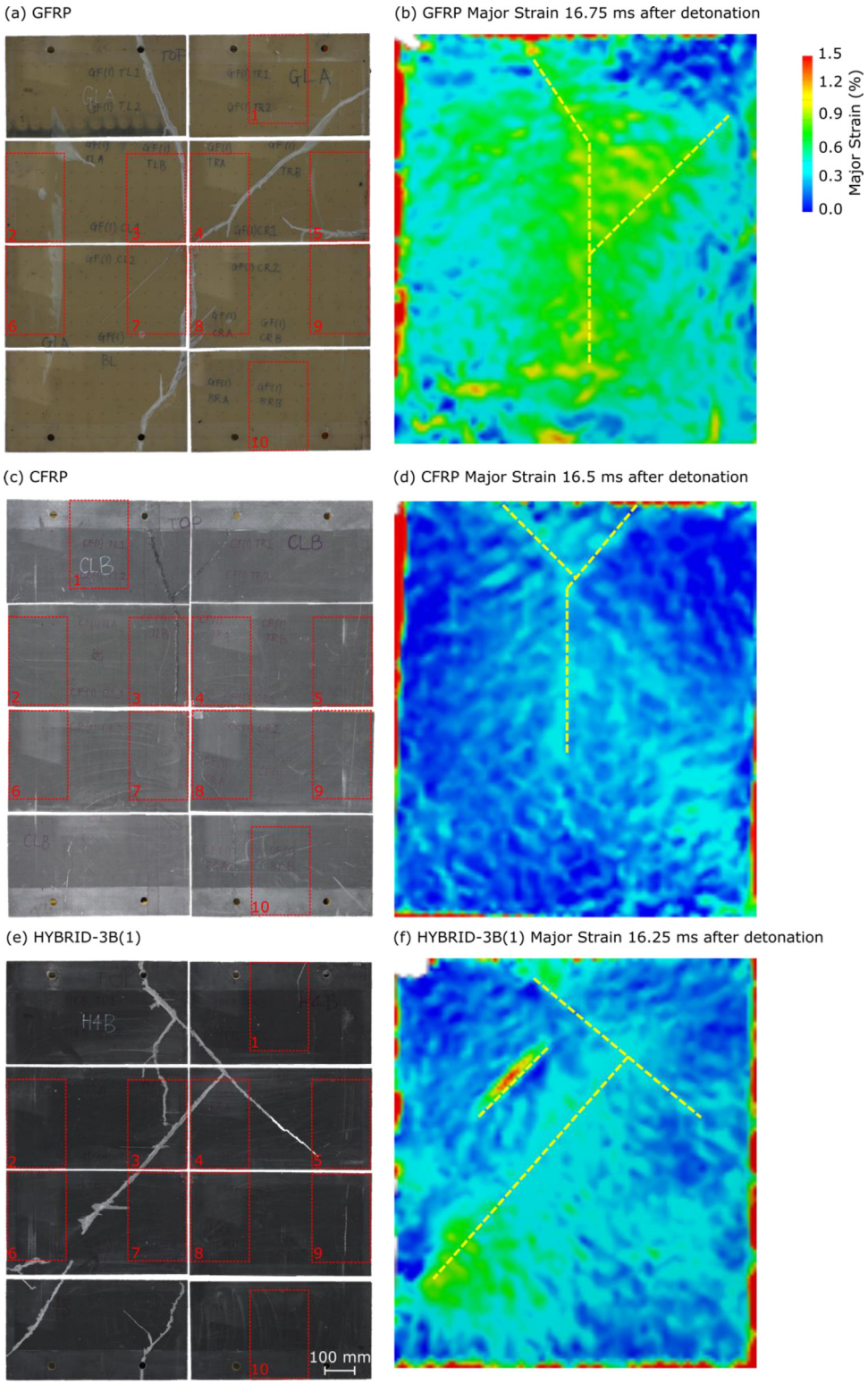

Fig. 14. Photographs showing the front skin following blast of (a) GFRP, (c) CFRP and (e) Hybrid-3B(1) and their DIC major strains respectively. The red dashed boxes highlight the sections removed for edgewise compression testing. (For interpretation of the references to colour in this figure legend, the reader is referred to the web version of this article.)

tested, carbon-fibres are far stronger than glass-fibres and it can be deduced that the percentage drop in the CFRP strength is greater than for the GFRP panel. Under these blast conditions, the higher stiffness of carbon-fibres is detrimental to post-blast panel performance.

The range of compressive strength results for the Hybrid-3B(1) panel is lower than either CFRP or GFRP demonstrating a more equal distribution of damage across the panel. Additionally, the mean compressive strength is greater for Hybrid-3B(1). Hybrid-3B(1) should lie between GFRP and CFRP, however, these results indicate that Hybrid-3B(1) is a more optimal choice for post-blast performance.

X-ray micro-CT scanning of the coupons from these three panels highlight significant differences in the damage sustained during blast and account for the differences in residual strength. Fig. 18(a) shows a

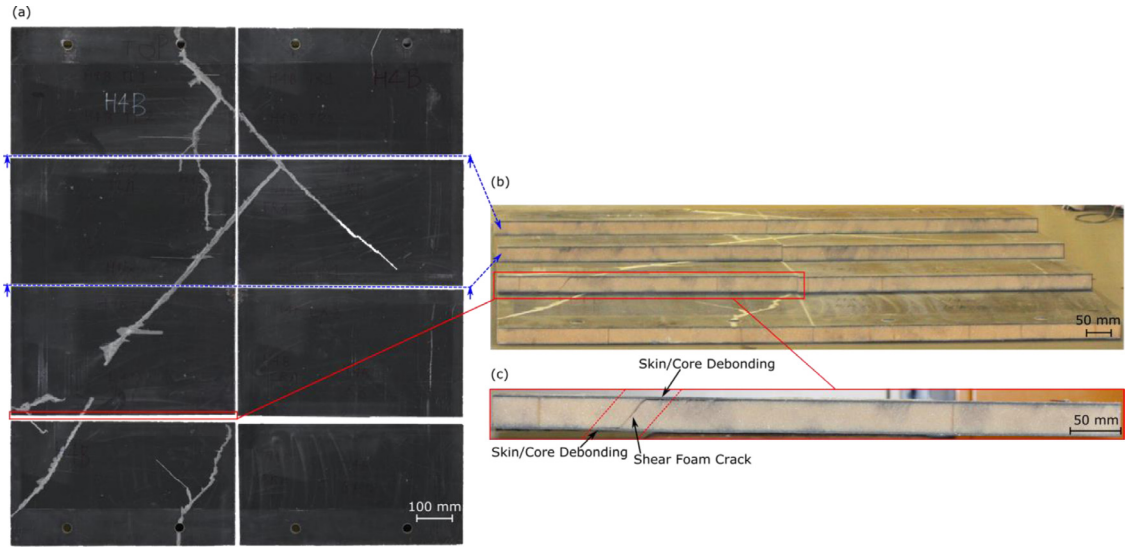

Fig. 15. Photographs showing the damage to the core of Hybrid-3B(1) as viewed from the bottom.

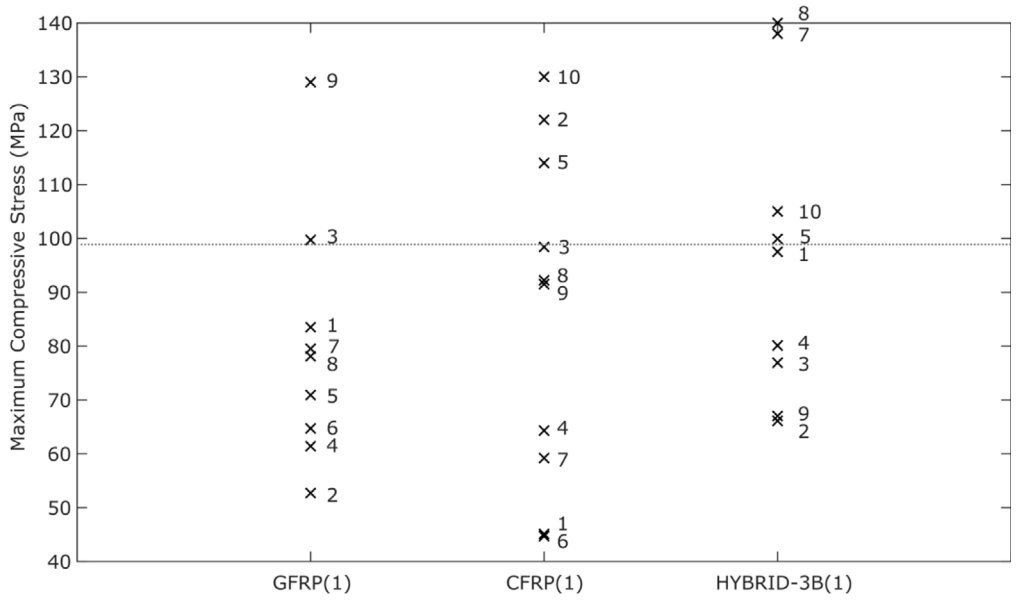

Fig. 16. Post-blast maximum compressive strength for the ten specimens taken from GFRP, CFRP and Hybrid-3B(1).

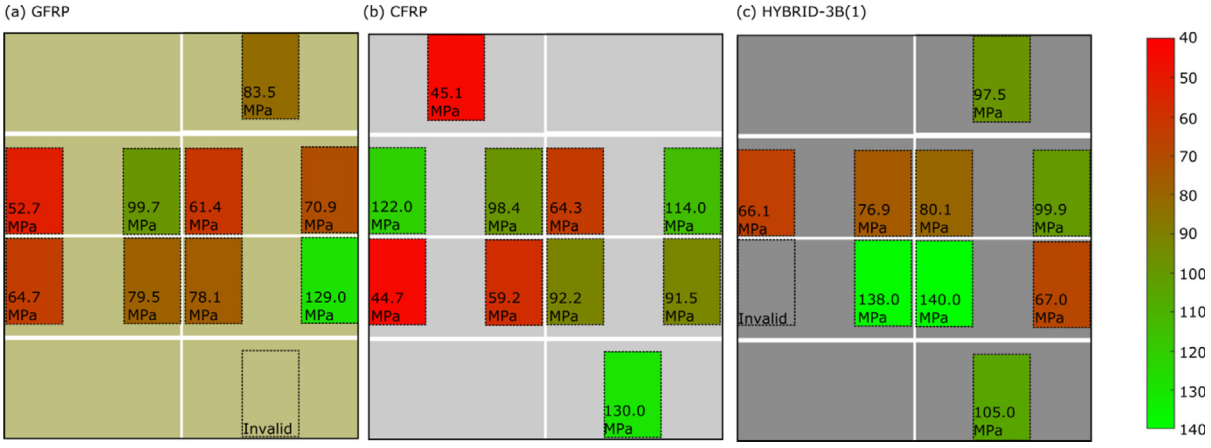

Fig. 17. Diagrams showing the compressive strength of specimens taken from various locations following blast of (a) GFRP, (b) CFRP and (c) Hybrid-3B(1) panels.

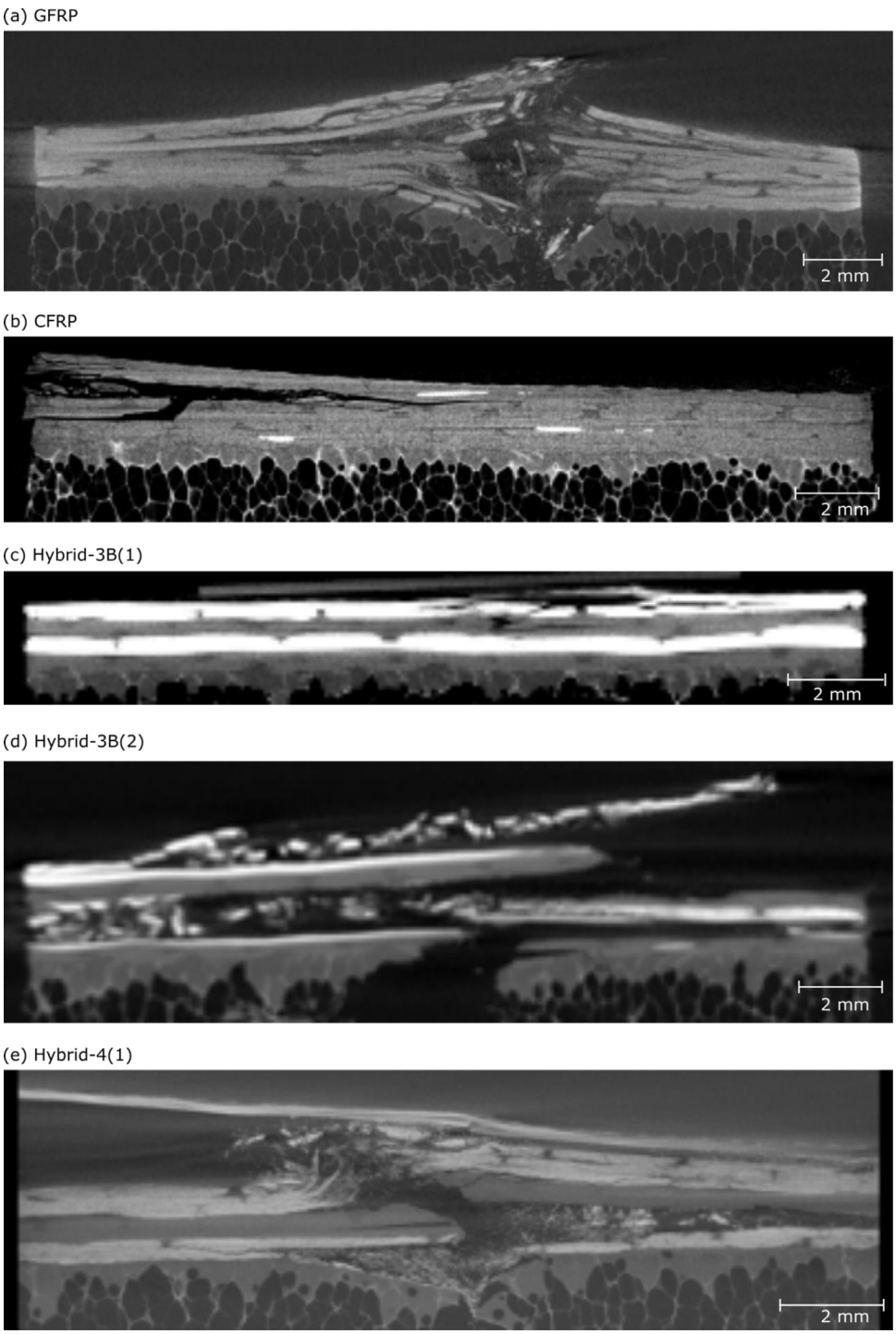

Fig. 18. X-ray micro-CT slices of (a) GFRP, (b) CFRP, (c) Hybrid-3B(1) from test series A and (d) Hybrid-3B(2), (e) Hybrid-4(1) from test series B.

through thickness crack propagating through the thickness of the GFRP panel from front surface to back surface of the skin. The CFRP panel suffers from delamination and cracking, as shown in Fig. 18(b). However, the crack does not traverse continuously through the thickness of the skin. The cracks step through each ply, propagating as delamination before cracking through the ply thickness again in subsequent slices of the X-ray micro-CT scan. Each layer within the CFRP skin does have a crack. Hybrid-3B(1) exhibits delamination in all plies except the inner layer of glass-fibre. Cracks are arrested before reaching this glass-fibre layer either from the external side or internal side and there is no damage path through the thickness of Hybrid-3B(1). By retaining the integrity of this ply, Hybrid-3B(1) is able to undergo greater work done and exhibits a greater mean residual compressive strength. Considering the results detailed, Hybrid-3B(1) offers advantages over conventional GFRP and CFRP panels under these test conditions.

4.2.2. Test series B: Hybrid-3B versus Hybrid-4 comparison

The front views of Hybrid-3B(2) and Hybrid-4(1) are shown in Fig. 19. The 300 mm × 200 mm specimen with varying amounts of damage that were removed from the panel for edgewise compression are shown by the red dashed boxes. Hybrid-4(1) suffers from a severe front skin crack travelling vertically from one bolt hole to another. This front skin damage directly correlates with the sharp gradient

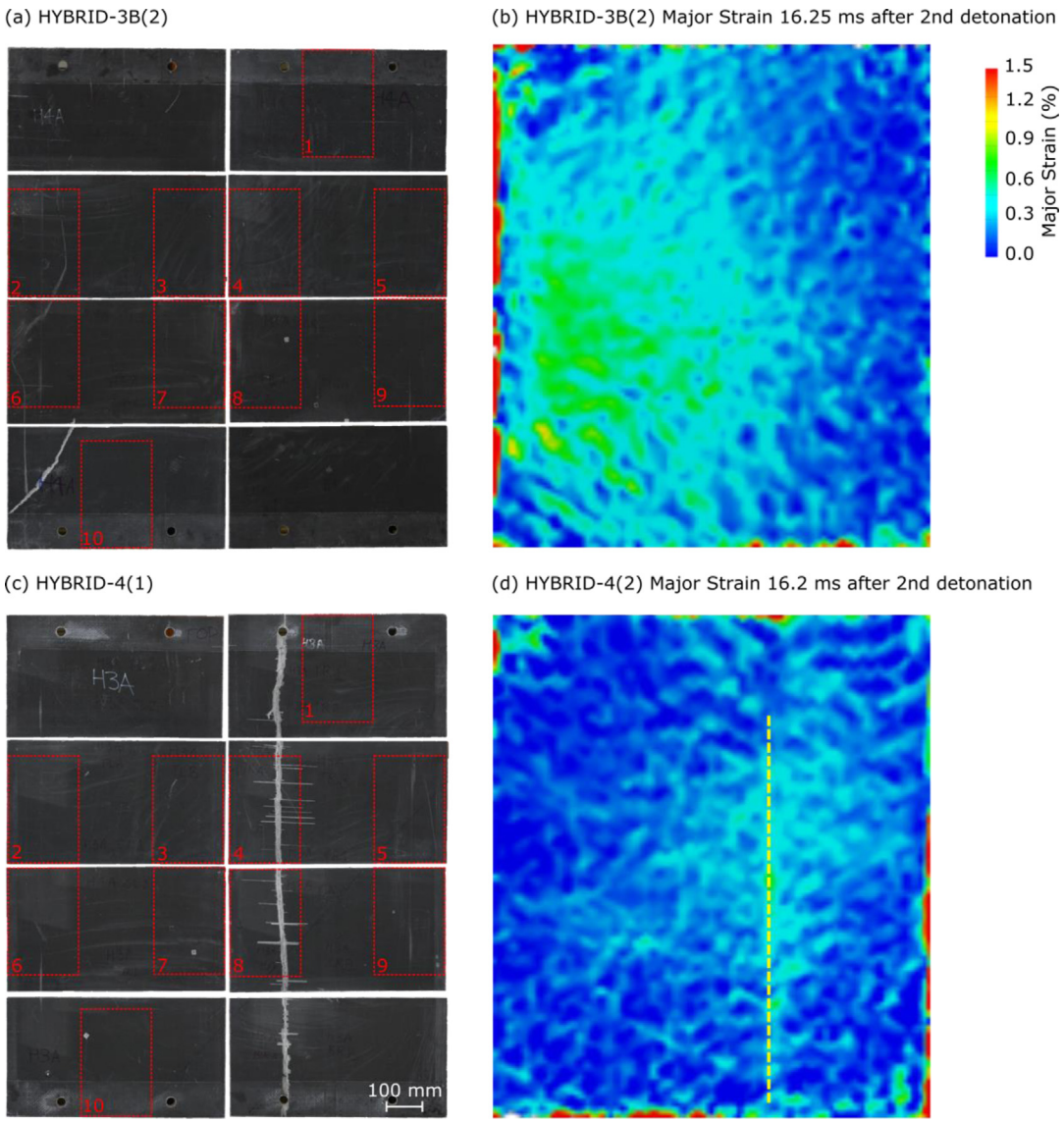

Fig. 19. Photographs showing the front skin following blast of (a) Hybrid-3B(2) and (c) Hybrid-4(1) and their DIC major strains respectively. The red dashed boxes highlight the sections removed for edgewise compression testing. (For interpretation of the references to colour in this figure legend, the reader is referred to the web version of this article.)

Table 6
Visual inspection of damage sustained by the panels in test series B.

Panel type	No. of core cracks	Length of core cracks (mm)	No. of core/front skin debonds	Length of front debonds (mm)	No. of core/rear skin debonds	Length of rear debonds (mm)	Length of front skin cracks (mm)
Hybrid-3B(2)	7	270	1	29	0	0	320
Hybrid-4(1)	8	305	3	77	0	0	1368

discontinuity and strain peak observed in the DIC analysis of Hybrid-4(1). Hybrid-3B(2) has a greater proportion of carbon-fibre leading to higher panel stiffness and lower deflection under blast loading. The damage inspection has revealed that this also leads to less visually observable damage (see Table 6).

Fig. 20 shows a plot of the maximum compressive strength for the specimen taken from the same locations on both panels. Two Hybrid-3B(2) specimens have a significantly lower strength. These specimens were taken from the left-hand side of Hybrid-3B(2) which was the outside edge of the cubicle. This edge experienced greater constraint and increased strain, as shown in Fig. 19, accounting for the damage. However, the specimen taken from the equivalent position on Hybrid-4(1), did not sustain the same amount of damage. Hybrid-4(1) suffers from a front skin crack spanning the length of the panel and spanning the length of two compression specimens. This skin crack and resulting core crack could have acted as a stress relief and could account for the lower damage identified on the constrained side of Hybrid-4(1). However, the presence of the crack does not dominate the compression results for these two Hybrid-4(1) specimens. The mean compressive strengths for Hybrid-3B(2) and Hybrid-4(1) are 96.6 MPa and 112.7 MPa, respectively. The ranges are 106.6 MPa and 60.7 MPa for Hybrid-3B(2) and Hybrid-4(1). As shown in Fig. 21, there is no clear correlation between the location from which the specimen was taken and the compressive strength achieved.

These results highlight that shear core cracking in Hybrid-3B(2) has a greater effect on post-blast compressive strength than skin failure and direct core cracking in Hybrid-4(1). Overall, the two hybrid types achieve similar mean compressive strengths, however, the

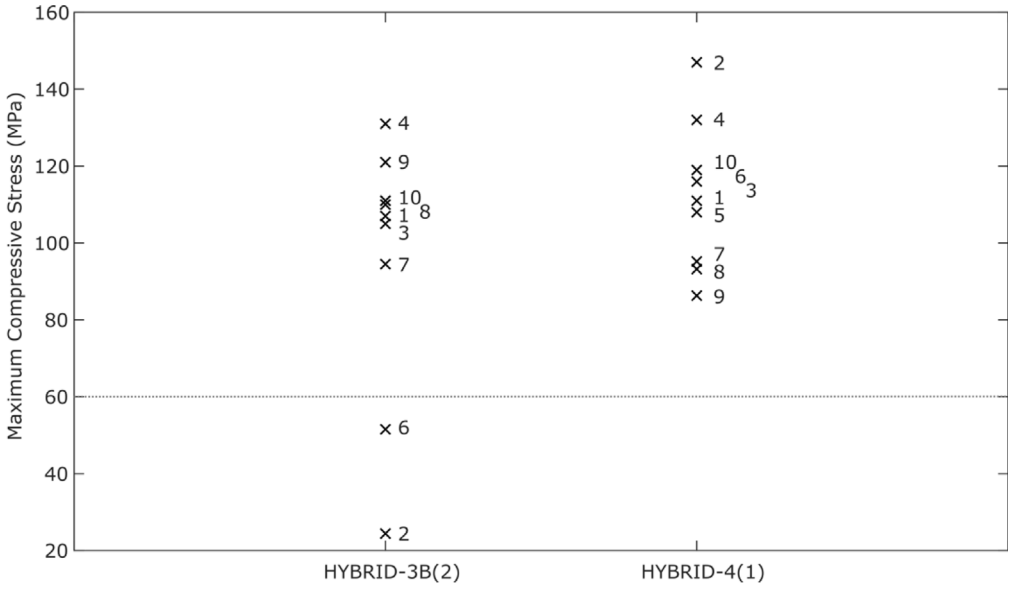

Fig. 20. Post-blast maximum compressive strength for the ten specimens taken from Hybrid-3B(2) and Hybrid-4(1).

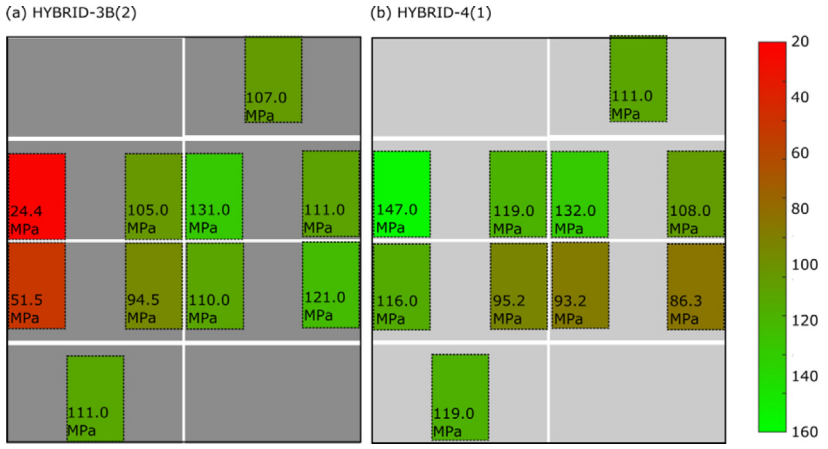

Fig. 21. Diagrams showing the compressive strength of specimens taken from various locations following blast of (a) Hybrid-3B(2) and (b) Hybrid-4(1) panels.

two more damaged Hybrid-3B(2) specimens detailed skew the range of Hybrid-3B(2) compressive strengths. Despite the severe front skin crack, Hybrid-4(1) more equally distributes blast damage across the panel.

X-ray micro-CT scanning of the coupons from these panels is also shown in Fig. 18. Hybrid-3B(2) exhibits a catastrophic through skin thickness crack which significantly affects the glass-fibre layers and the underlying foam core. This specimen was taken from the left-hand side of the panel and accounts for the significant drop in residual compressive strength in this region. Fig. 18(e) shows a through thickness crack propagating through the thickness of the Hybrid-4(1) panel with evidence of delamination and some crack stepping. Although Hybrid-4(1) visibly has a crack running the length of the panel, the severity of the damage is reduced compared to Hybrid-3B(2) which accounts for the improved post-blast performance of the panel. Under these test conditions, Hybrid-4(1) is advantageous with an increased residual compressive strength, smaller range, indicating more uniform distribution of damage across the panel, and reduced severity of damage in locations where cracking does occur. However, key considerations of service loads and damage mechanisms is needed before recommendations can be made over layups and preferential damage mechanisms against blast.

5. Conclusions

Five composite sandwich panels were subjected to air blast loads. The investigations were carried out to compare the blast resilience of different hybrid skin layups along with their performance under different blast severities and repeat loads. Although direct comparisons between panels were intended, the complex nature of blast experiments resulted in variability and complications. For example, Hybrid-3B(1) underwent an 85% greater blast impulse compared to GFRP and CFRP due to an almost double positive phase duration. Despite this, the deflection of Hybrid-3B(1) was found to lie between that of GFRP and CFRP, as expected from their panel bending stiffnesses.

Hybrid-3B(1) sustained a similar extent of damage and a greater mean post-blast compressive strength compared to both GFRP and CFRP. In addition, the range of post-blast compressive strengths across Hybrid-3B(1) were smaller, showing a more uniform distribution of damage across the panel. Considering Hybrid-3B(1) underwent a greater impulse, the results indicate that Hybrid-3B(1) is a more optimal choice for post-blast performance. Furthermore, X-ray micro-CT scanning of test samples demonstrated the type of energy absorption mechanisms that can occur in each skin layup. The GFRP panel exhibits a crack propagating through the thickness of the GFRP panel from

front surface to back surface of the skin. The CFRP panel suffers from delamination and cracking. Although the crack does not traverse continuously through the thickness of the skin, the cracks do step through each ply, propagating as delamination before cracking through the ply thickness again. Hybrid-3B(1) exhibits delamination in all plies except the inner layer of glass-fibre. All cracks are arrested before reaching this glass-fibre layer either from the external side or internal side and there is no damage path through the thickness of Hybrid-3B(1). This indicates that interactions between the skin layers prevents a direct through thickness crack. By redirecting the crack and causing delamination, debonding and fibre breakage, energy is absorbed by the hybrid skin. Retaining the integrity of this ply accounts for the superior post-blast performance of the Hybrid-3B(1) panel.

In test series B, although Hybrid-4(1) suffers from a crack spanning the length of the panel, this crack acts as a stress relief and allows for a more equal distribution of blast damage across the panel. Although this crack does not significantly affect the post-blast compressive performance of Hybrid-4(1), it is undesirable in marine applications due to potential water ingress. Furthermore alternative subsequent loading regimes may uncover undesirable load bearing capacity due to this damage mechanism. The higher bending stiffness of Hybrid-3B(2) results in a less compliant panel which leads to severe damage in the edge that experienced greater constraint. X-ray micro-CT analysis of specimens from each panel reveal that repeat blast loading exacerbates damage and causes through skin thickness cracking in both hybrid panels. The damage sustained in Hybrid-3B(2) is more severe than the damage in Hybrid-4(1). Under these blast conditions, Hybrid-4(1) is a more optimised layup for during and post-blast performance. However, further work is required to prevent the significant skin crack in Hybrid-4(1) from occurring whilst retaining the advantages of the layup. In addition, testing of Hybrid-4(1) against conventional panels under blast conditions representative of the final application is recommended.

Additionally, the experiments have revealed that DIC deflection maps and cross-sections accurately capture the location of severe damage and, equally, severe front skin damage has a significant effect on panel deflection. As previously outlined in Ref. [36], the support conditions dictate the location of core cracks. The rigidity of the support conditions results in high bending moments causing core cracks to occur. The fixing method, bolts and bolt holes, act as the initiation locations for front skin cracks. The design of the support structure can significantly aid in blast resilience and a holistic approach considering both panels and support should be taken when designing for blast resilience. Furthermore, with accurate modelling of the support structure, relative performance of panel materials is feasible [28] allowing for information to be extracted and shared and avoiding test specific results.

CRediT authorship contribution statement

E. Rolfe: Writing – original draft, Visualization, Methodology, Investigation. **R. Quinn:** Validation, Investigation. **G. Irven:** Investigation. **D. Brick:** Resources, Investigation. **R.E. Johnston:** Writing – review & editing, Investigation, Funding acquisition. **J.P. Dear:** Writing – review & editing, Supervision, Funding acquisition, Conceptualization. **H. Arora:** Writing – review & editing, Supervision, Methodology, Investigation, Funding acquisition, Conceptualization.

Declaration of competing interest

The authors declare the following financial interests/personal relationships which may be considered as potential competing interests: Emily Rolfe reports financial support was provided by Office of Naval Research. Emily Rolfe reports financial support was provided by Engineering and Physical Sciences Research Council. Hari Arora reports financial support was provided by Engineering and Physical Sciences Research Council. Hari Arora reports financial support was provided by Ser Cymru National Research Network ICA. Richard E Johnston reports financial support was provided by Engineering and Physical Sciences Research Council. Richard E Johnston reports financial support was provided by Welsh Government. Richard E Johnston reports financial support was provided by European Social Fund.

Data availability

Data will be made available on request.

Acknowledgements

The authors would like to thank Dr Yapa Rajapakse of the Office of Naval Research, United States [N62909-15-1-2004] for supporting Dr Emily Rolfe, Dr Mark Kelly and Dr Hari Arora during their PhDs and EPSRC, United Kingdom for supporting Dr Emily Rolfe. The authors also acknowledge the support from the Sêr Cymru National Research Network Industrial Collaboration Award, United Kingdom, which supported instrumentation costs to the project. The damage analysis work was funded by UK EPSRC, through the Impact Acceleration Account 2020–2022, administered by Swansea University. The micro-CT work was supported by the Advanced Imaging of Materials (AIM), United Kingdom core facility [EPSRC Grant No. EP/M028267/1], the Welsh Government Enhancing Competitiveness Grant, United Kingdom [MA/KW/5554/19] and the European Social Fund (ESF) through the European Union's Convergence programme administered by the Welsh Government. The RWIF Collaboration Booster R3-EEF37 supported discussions on composite materials. The assistance throughout the experiments from Dr Alex Fergusson of FAC Technology, Mark Johnson of Slowmo Ltd, Amy Johnson of GOM UK and Dr Jun Liu of Imperial College London was very much appreciated. The authors would also like to thank Radnor Range Ltd for the in-kind support provided for blast testing.

For the purpose of open access, the authors have applied a Creative Commons Attribution (CCBY) licence to any Author Accepted Manuscript version arising.

References

[1] AP. Mouritz, E. Gellert, P. Burchill, K. Challis, Review of advanced composite structures for naval ships and submarines, Compos. Struct. 53 (2001) 21–42, http://dx.doi.org/10.1016/S0263-8223(00)00175-6.

[2] GS. Langdon, D. Karagiozova, CJ. von Klemperer, GN. Nurick, A. Ozinsky, EG. Pickering, The air-blast response of sandwich panels with composite face sheets and polymer foam cores: Experiments and predictions, Int. J. Impact Eng. 54 (2013) 64–82, http://dx.doi.org/10.1016/J.IJIMPENG.2012.10.015.

[3] SA. Tekalur, AE. Bogdanovich, A. Shukla, Shock loading response of sandwich panels with 3-D woven E-glass composite skins and stitched foam core, Compos. Sci. Technol. 69 (2009) 736–753, http://dx.doi.org/10.1016/J.COMPSCITECH.2008.03.017.

[4] E. Wang, N. Gardner, A. Shukla, The blast resistance of sandwich composites with stepwise graded cores, Int. J. Sol. Struct. 46 (2009) 3492–3502, http://dx.doi.org/10.1016/J.IJSOLSTR.2009.06.004.

[5] AP. Mouritz, Advances in understanding the response of fibre-based polymer composites to shock waves and explosive blasts, Composites A 125 (2019) 305–315, http://dx.doi.org/10.1016/j.compositesa.2019.105502.

[6] ZW. Guan, A. Aktas, P. Potluri, WJ. Cantwell, G. Langdon, GN. Nurick, The blast resistance of stitched sandwich panels, Int. J. Impact Eng. 65 (2014) 137–145, http://dx.doi.org/10.1016/J.IJIMPENG.2013.12.001.

[7] M. Kelly, H. Arora, A. Worley, M. Kaye, P. Del Linz, PA. Hooper, JP. Dear, Sandwich panel cores for blast applications: Materials and graded density, Exp. Mech. (2015) 1–22, http://dx.doi.org/10.1007/s11340-015-0058-5.

[8] SA. Tekalur, K. Shivakumar, A. Shukla, Mechanical behavior and damage evolution in E-glass vinyl ester and carbon composites subjected to static and blast loads, Composites B 39 (2008) 57–65, http://dx.doi.org/10.1016/J.COMPOSITESB.2007.02.020.

[9] A. Gargano, K. Pingkarawat, M. Blacklock, V. Pickerd, AP. Mouritz, Comparative assessment of the explosive blast performance of carbon and glass fibre-polymer composites used in naval ship structures, Compos. Struct. 171 (2017) 306–316, http://dx.doi.org/10.1016/J.COMPSTRUCT.2017.03.041.

[10] A. Kerber, A. Gargano, K. Pingkarawat, AP. Mouritz, Explosive blast damage resistance of three-dimensional textile composites, Composites A 100 (2017) 170–182, http://dx.doi.org/10.1016/J.COMPOSITESA.2017.05.005.

[11] H. Arora, Blast Loading of Fibre Reinforced Polymer Composite Structures, Imperial College London, 2011.
[12] H. Arora, M. Kelly, A. Worley, P. Del Linz, A. Fergusson, PA. Hooper, JP. Dear, Compressive strength after blast of sandwich composite materials, Philos. Trans. R. Soc. Lond. A Math. Phys. Eng. Sci. (2014) 372, http://rsta.royalsocietypublishing.org/content/372/2015/20130212.abstract.
[13] M. Hoo Fatt, X. Ouyang, RJ. Dinan, Blast response of walls retrofitted with elastomer coatings, in: Struct. under Shock Impact VIII Proc. Eighth Int. Conf. Struct. under Shock Impact, 2004, pp. 129–138.
[14] N. Gardner, E. Wang, P. Kumar, A. Shukla, Blast mitigation in a sandwich composite using graded core and polyurea interlayer, Exp. Mech. 52 (2012) 119–133, http://dx.doi.org/10.1007/s11340-011-9517-9.
[15] Y. Swolfs, L. Gorbatikh, I. Verpoest, Fibre hybridisation in polymer composites: A review, Composites A 67 (2014) 181–200, http://dx.doi.org/10.1016/j.compositesa.2014.08.027.
[16] E. Sevkat, B. Liaw, F. Delale, BB. Raju, Drop-weight impact of plain-woven hybrid glass–graphite/toughened epoxy composites, Composites A 40 (2009) 1090–1110, http://dx.doi.org/10.1016/J.COMPOSITESA.2009.04.028.
[17] E. Sevkat, B. Liaw, F. Delale, BB. Raju, Effect of repeated impacts on the response of plain-woven hybrid composites, Composites B 41 (2010) 403–413, http://dx.doi.org/10.1016/J.COMPOSITESB.2010.01.001.
[18] A. Enfedaque, JM. Molina-Aldareguía, F. Gálvez, C. González, J. LLorca, Effect of glass fiber hybridization on the behavior under impact of woven carbon fiber/epoxy laminates, J. Compos. Mater. 44 (2010) 3051–3068, http://dx.doi.org/10.1177/0021998310369602.
[19] KS. Pandya, JR. Pothnis, G. Ravikumar, NK. Naik, Ballistic impact behavior of hybrid composites, Mater. Des. 44 (2013) 128–135, http://dx.doi.org/10.1016/j.matdes.2012.07.044.
[20] E. Randjbaran, R. Zahari, NA. Abdul Jalil, DL. Abang Abdul Majid, Hybrid composite laminates reinforced with kevlar/ carbon/ glass woven fabrics for ballistic impact testing, Sci. World J. (2014) 413–753, http://dx.doi.org/10.1155/2014/413753.
[21] R. Park, J. Jang, Effect of laminate geometry on impact performance of aramid fiber/ polyethylene fiber hybrid composites, J. Appl. Polym. Sci. (ISSN: 0021-8995) 75 (2000) 952–959.
[22] G. Czél, MR. Wisnom, Demonstration of pseudo-ductility in high performance glass/epoxy composites by hybridisation with thin-ply carbon prepreg, Composites A 52 (2013) 23–30, http://dx.doi.org/10.1016/j.compositesa.2013.04.006.
[23] P. Suwarta, M. Fotouhi, G. Czél, M. Longana, MR. Wisnom, Fatigue behaviour of pseudo-ductile unidirectional thin-ply carbon/epoxy-glass/epoxy hybrid composites, Compos. Struct. (2019) 224, http://dx.doi.org/10.1016/j.compstruct.2019.110996.
[24] M. Fotouhi, M. Jalalv, M. Saeedifar, B. Xiao, MR. Wisnom, High performance quasi-isotropic thin-ply carbon/glass hybrid composites with pseudo-ductile behaviour loaded off-axis, Compos. Struct. (2020) 247, http://dx.doi.org/10.1016/j.compstruct.2020.112444.
[25] G. Idarraga, M. Jalalv, M. Fotouhi, J. Meza, MR. Wisnom, Gradual failure in high-performance unidirectional thin-ply carbon/glass hybrid composites under bending, Compos. Struct. (2021) 271, http://dx.doi.org/10.1016/j.compstruct.2021.114128.
[26] E. Rolfe, R. Quinn, A. Sancho, C. Kaboglu, A. Johnson, H. Liu, PA. Hooper, JP. Dear, H. Arora, Blast resilience of composite sandwich panels with hybrid glass-fibre and carbon-fibre skins, Multisc. Multidiscip. Model. Exp. Des. 1 (2018) 197–210, http://dx.doi.org/10.1007/s41939-018-0025-9.
[27] E. Rolfe, R. Quinn, G. Irven, D. Brick, JP. Dear, H. Arora, Underwater blast loading of partially submerged sandwich composite materials in relation to air blast loading response, Int. J. Lightweight Mater. Manuf. 4 (2020) 387–402, http://dx.doi.org/10.1016/j.ijlmm.2020.06.003.
[28] E. Rolfe, C. Kaboglu, R. Quinn, PA. Hooper, H. Arora, JP. Dear, High velocity impact and blast loading of composite sandwich panels with novel carbon and glass construction, J. Dyn. Behav. Mater. 4 (2018) 359–372, http://dx.doi.org/10.1007/s40870-018-0163-5.
[29] SE. Rigby, A. Tyas, T. Bennett, SD. Fay, SD. Clarke, JA. Warren, A numerical investigation of blast loading and clearing on small targets, Int. J. Prot. Struct. 5 (3) (2014) 253–274, http://dx.doi.org/10.1260/2041-4196.5.3.253.
[30] EW. Andrews, NA. Moussa, Failure mode maps for composite sandwich panels subjected to air blast loading, Int. J. Impact Eng. 36 (2009) 418–425, http://dx.doi.org/10.1016/j.ijimpeng.2008.08.005.
[31] S. Forth, ProSAir 2018, 4 User Guide, 2018.
[32] TA. Rose, A computational tool for air blast calculations: Air3d version 9 users' guide, 2006.
[33] M. Kelly, Comparing the Blast Tolerance of Different Composite Structures, Imperial College London, 2016, http://dx.doi.org/10.25560/40428.
[34] D. Zenkert, A. Shipsha, P. Bull, B. Hayman, Damage tolerance assessment of composite sandwich panels with localised damage, Compos. Sci. Technol. 65 (2005) 2597–2611, http://dx.doi.org/10.1016/j.compscitech.2005.05.026.
[35] GN. Nurick, GS. Langdon, Y. Chi, N. Jacob, Behaviour of sandwich panels subjected to intense air blast – Part 1: Experiments, Compos. Struct. 91 (2009) 433–441, http://dx.doi.org/10.1016/j.compstruct.2009.04.009.
[36] H. Arora, PA. Hooper, JP. Dear, Dynamic response of full-scale sandwich composite structures subject to air-blast loading, Composites A 42 (2011) 1651–1662, http://dx.doi.org/10.1016/j.compositesa.2011.07.018.